

An Analysis of Unmanned Aerial Vehicle-Based Acoustic Atmospheric Tomography

Anthony Finn and Kevin J. Rogers

School of Engineering, University of South Australia, Australia

ABSTRACT

The engine of an unmanned aerial vehicle generates acoustic energy comprising multiple prominent narrowband tones superimposed onto a broadband background. This signature may be synchronously observed both onboard the aircraft and by a set of microphones on the ground. Comparison of the projected and observed signals allows computation of atmospheric sound speed values for a set of intersecting rays. Tomography may then be used to estimate spatially varying temperature and wind velocity profiles of the intervening medium. Errors in these atmospheric reconstructions are a function of several factors, which include: refraction, multi-path, atmospheric turbulence, position and velocity errors, instrumental errors in the measurement of the signals, and statistical uncertainty in processing techniques used to perform the signature comparisons. Vertical cross-sections of weakly-sheared daytime convective atmospheric boundary layers, created using large eddy simulation code, are combined with error models of the geometry, propagation and instruments to determine levels of inaccuracy that can be tolerated for faithful reconstruction of target atmospheres.

1. INTRODUCTION

The *inverse problem* may be described as using measurements of observed parameters to infer values of model parameters. In general, therefore, the inverse problem is the reconstruction of a model of a system represented by \mathbf{m} from a set of observations denoted by \mathbf{b}_{obs} . The model and the data set are related by a set of explicit equations, $\mathbf{b}_{obs} = \mathbf{a}(\mathbf{m})$, which may be written as, $\mathbf{b}_{obs} = \mathbf{A}\mathbf{m}$, if the relationship between model parameters is linear (where \mathbf{A} is the data kernel). It is typical for a set of observations to over-determine some model parameters and under-determine others. This is generally due to the uneven nature of the sounding of a medium under investigation or noisy data.

In this paper the system under investigation is the atmosphere, specifically temperature and wind vector profiles computed from sound speed observations using the natural acoustic signature of an unmanned aerial vehicle (UAV) and an inverse technique known as *tomography*. Tomography is a sub-set inverse theory from which the data kernel is formed by integrating the model parameters along the ray paths that intersect the medium. That is,

$$b_i = \int_{r_i} m(\vec{r}) d\vec{r}, \quad (1)$$

where \vec{r}_i is the i^{th} ray path. To overcome the limitations of the continuous representation we traditionally discretise the system under investigation and re-write Eq. (1) as,

$$b_i = \sum_j A_{ij} m_j, \quad (2)$$

which is similar in form to $\mathbf{b}_{obs} = \mathbf{A}\mathbf{m}$. If the wind and temperature fields are linearized about mean values T_0 and \mathbf{V}_0 , the travel time, t_{pj} , for sound ray(j) is given by

$$t_{pj} = \frac{l_j}{c_0} \left(1 - \frac{\mathbf{V}_0 \cdot \mathbf{v}_{ray}}{c_0} \right) - \int_0^{l_j} \left(\frac{\Delta T(\mathbf{X}(l))}{2T_0 c_0} + \frac{\Delta \mathbf{V}(\mathbf{X}(l)) \cdot \mathbf{v}_{ray}}{c_0^2} \right) dl, \quad (3)$$

where l_j is the path distance, from $X_u(l) = (x_u(l), y_u(l), z_u(l))$ the location of the UAV, to $X_r(l) = (x_r(l), y_r(l), z_r(l))$ the location of the receiver, c_0 is mean sound speed, \mathbf{V}_0 is mean wind speed vector over the volume, $\Delta T(\mathbf{X})$ is (time-averaged) temperature deviation at location \mathbf{X} , $\Delta \mathbf{V}(\mathbf{X}) = [\Delta V_x, \Delta V_y, \Delta V_z]$ is (time-averaged) wind speed deviation at location \mathbf{X} and dl an integration length along the ray path.

It is also possible to express the state of the atmosphere at a given time and location as a linear combination of a two independent sets of radial basis functions (RBF), $\Delta T(\mathbf{X})$ and $\Delta \mathbf{V}(\mathbf{X})$, (Wiens and Behrens 2009, R. Aster 2013, Rogers and Finn 2013), which are 2- or 3D Gaussian functions of the form $\phi(r) = e^{-kr^2}$, where r is the distance from the RBF spatial centre and k is a scaling factor that is the same for all RBFs and all networks. If the RBF centres \mathbf{X}_{cj} are distributed evenly inside a lattice described by the UAVs' flight paths, the temperature and wind fields may be approximated by

$$\Delta T(\mathbf{X}) = \sum_{j=1}^{N_r} W_{Tj} e^{-k\|\mathbf{X}-\mathbf{X}_{cj}\|^2} \tag{4}$$

$$\Delta \mathbf{V}(\mathbf{X}) = \sum_{j=1}^{N_r} \mathbf{W}_j e^{-k\|\mathbf{X}-\mathbf{X}_{cj}\|^2} \tag{5}$$

where N_r is the number of RBF centres, A_{Tj} the temperature weighting coefficient for $RBF(j)$ and $\mathbf{A}_j = [A_{jx}, A_{jy}, A_{jz}]$ the wind weighting coefficient vector for $RBF(j)$ in the x , y , and z directions. These equations may be expressed in matrix notation, $F(\mathbf{X}) = \Phi(\mathbf{X})\mathbf{A}$, where $F(\mathbf{X}) = [\Delta T(\mathbf{X}), \Delta V_x, \Delta V_y, \Delta V_z]^T$ is a (4×1) column vector of temperature and wind speed component deviations (x , y , z), \mathbf{A} is a $[4N_r \times 1]$ column vector of parameter weights and $\Phi(\mathbf{X})$ is a $[4N_r \times 4]$ matrix of RBFs. Although this method is neither the only inversion technique available, nor one shown to perform better than any other, it significantly reduces the number of model parameters such that the system is over-determined and can be solved directly by least squares as the model parameters are now the RBF coefficients.

Such tomographic techniques have been used for decades in oceanography, medicine, archaeology and the remote sensing of various geophysical media (Munk and Wunsch 1979, Cornuelle 1982, Kak and Slaney 2001). It allows the internal structure of a medium to be visualised based on interactions between it and energy emitted by appropriately located transmitters. Its first application to atmospheric observation was based on signals transmitted and received between a series loud speakers and microphones mounted on a series of masts covering an area of 200 x 240 m (Wilson and Thomson 1994). Sound speeds were computed for ray paths passing through the intervening atmosphere and temperature and wind velocity profiles then estimated. Other arrays have since been built (Arnold, Ziemann et al. 1999, Ziemann, Arnold et al. 1999, Jovanovic, Sbaiz et al. 2009), some of which allow 3D tomography (Wilson, Ziemann et al. 2001, Vecherin, Ostashev et al. 2008). Several tomographic techniques have been developed (Spiesberger and Fristrup 1990, Vecherin, Ostashev et al. 2006, Vecherin, Ostashev et al. 2007, Vecherin, Ostashev et al. 2008, Vecherin, Ostashev et al. 2008, Barth and Raabe 2011, Kolouri and Azimi-Sadjadi 2012), including some that passively observe the atmosphere using noise sources such as birds, meteors and commercial aircraft (Spiesberger and Fristrup 1990, Ostashev, Voronovich et al. 2000, Wilson, Ziemann et al. 2001).

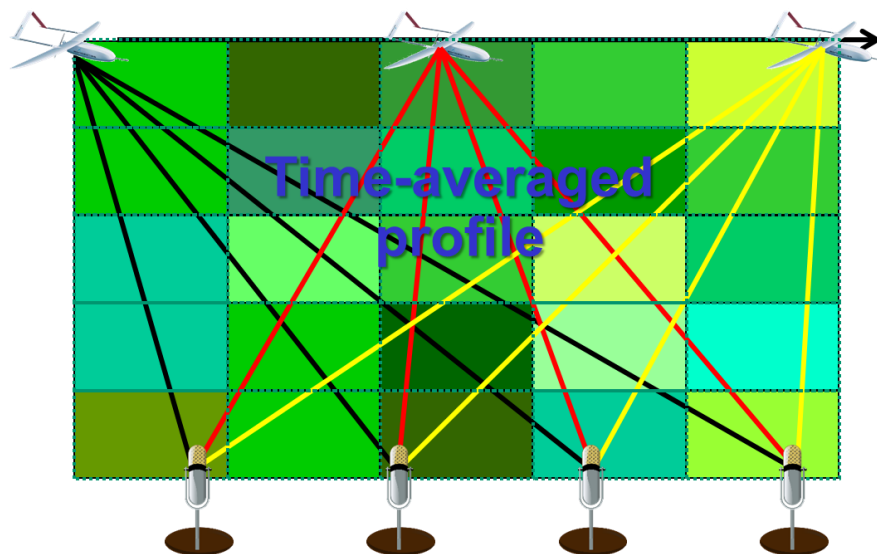


Figure 1: A graphical depiction of UAV-based acoustic atmospheric tomography, showing a lattice of (colour-coded) constant blocks of sound speed between microphones located on the ground and the (moving) UAV.

Acoustic atmospheric tomography (AAT) has practical application in several research fields. For example, processes of heat, moisture and momentum exchange occur between the earth's surface and the atmospheric surface layer, which extends up to about 100 m above the ground, and the atmospheric boundary layer (ABL), which extends up to 2 km. Thus, parameterization and development of models can improve weather forecasting and studies in climatology. Accumulation and short-range transfer of anthropogenic pollutants also occur within the ABL. Hence, to aid in environmental protection, it is necessary to examine mechanisms for turbulent mixing within this layer and observe its parameters. The ABL strongly affects the propagation of electromagnetic waves. Therefore data on ABL refractive index variations are also useful in understanding the nature of atmospheric interference in location and navigation systems and in line-of-sight communication links. Finally, wind shear in the lower part of the ABL can be dangerous for aircraft performing take-off and landing operations, so information on wind conditions in the ABL are of great importance to air transport safety.

More recently AAT techniques based on the overflight of unmanned aerial vehicle (UAV) have been developed (Finn and Franklin 2011, Finn and Franklin 2011, Rogers and Finn 2013, Rogers and Finn 2013, Rogers and Finn 2013, Finn, Rogers et al. 2014, Rogers and Finn 2014). The UAV-based approach offers several advantages over existing techniques and more traditional meteorological sensors such as cup and sonic anemometers, sound detection and ranging (SODAR), light detection and ranging (LIDAR), radio-acoustic sounder sending (RASS), satellite-based techniques, radar, and radio-sondes.

For example, some traditional instruments have relatively poor vertical resolution in the lower atmospheric layers and are not suitable for determining parameters in the ABL. Also, basic experimental data is often obtained with contact sensors mounted on masts, balloons and aircraft. Obviously, a complete volume of information, required for a comprehensive study of the ABL, cannot be obtained from such measurements. As the UAV has no pilot and low kinetic energy it can fly at altitudes from a few metres to several kilometres, in dangerous environments and for long periods. This enables parameterisation of the surface layer and ABL. UAV-based AAT also has disadvantages: as the UAV has finite speed the atmosphere changes over the observation period and the resulting inversion thus represents only a time-averaged profile.

The techniques employed in this paper are based on the time-frequency signal analysis of a propeller-driven aircraft and the reader is referred to (Rogers and Finn 2013, Rogers and Finn 2013, Rogers and Finn 2013, Finn, Rogers et al. 2014, Rogers and Finn 2014, Finn and Rogers 2015, Finn and Rogers 2016, Finn and Rogers 2016, Rogers and Finn 2016) for more details. In particular these papers describe the forward and inverse approaches used to obtain the tomographic reconstructions.

This paper is structured as follows: Section 2 discusses the results of simulations based on Large Eddy Simulation (LES) code; Section 3 describes the results of some comparative trials with a Fulcrum 3D SODAR; and Section 4 offers some concluding remarks.

2. PROFILE COMPARISONS BASED ON SIMULATED ATMOSPHERIC CONDITIONS

Simulating realistic atmospheric profiles is difficult because of the dominance of the non-linear flow effects and wide spectrum of scale sizes involved. Sullivan and Patton (Sullivan and Patton 2011) generated a suite of atmospheric simulations for a daytime convective ABL using large eddy simulation (LES). The volume of atmosphere represented was 5,120m x 5,120m (horizontal) x 2,048m (vertical) for a uniform grid mesh of $1,024^3$ points; and simulations were carried forward in time for 25 large eddy turnover times. The LES data set thus provides temperature and 3D wind velocity vector at each point in the space-time lattice. The equations and parameters used to simulate this weakly sheared daytime convective ABL are contained in (Sullivan and Patton 2011).

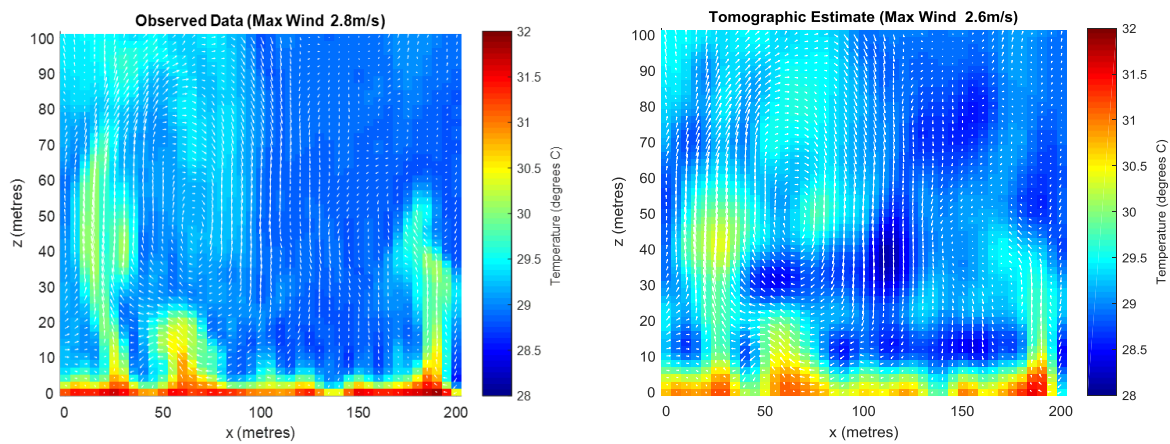


Figure 2: (left) cross-section of an atmospheric profile generated by Sullivan and Patton (Sullivan and Patton 2011) and (right) a tomographic reconstruction of the left hand image for a uniform lattice of RBF separated by 10m x 10m. The figures show temperature colour coded as per the bar on the right hand side and wind speed shown as arrows (note: we recommend softcopy/online versions if visibility of the arrows is required).

Figure 2 (left) shows a vertical cross-section of temperature and wind velocity through the LES data set over a baseline of 200m and up to an altitude of 100m. It is typical of that used in our analysis. Temperature is colour-coded according to the scale on the right of each image and arrows point in the direction of wind flow, with magnitude representing wind speed. The maximum wind speed is 2.7m/s. Although LES allows simulation of time-varying atmospheres, profiles were assumed to be frozen over the observation period.

Figure 2 (right) shows the tomographic reconstruction for a simulated linear array of ground sensors separated by 10m. The ray path sampling is commensurate for a UAV travelling at 28m/s and an acoustic payload capable of performing a 0.5s FFT, or 2^{16} samples at 44.1kHz with a 75% overlap between acoustic sample sets. The RBFs are set in a uniform 10m x 10m lattice, which limits the resolution of the technique against the target data set to 10m. The simulations of time delay contain no errors and the UAV flight path (out of picture) has flown from 50m to 100m and back again, i.e. in a trapezoid. Comparison between the left and right images allows examination of the fidelity with which the technique is potentially able to reconstruct the considerable variation in temperature in the lowest regions of the atmosphere, where for horizontal UAV overflights the ray paths are unable to intersect one another or the lower RBF centres.

There are, of course, many real-world sources of error, including: use of the ray path approximation, refraction, multi-path (e.g. from tall grasses, trees, shrubs, leaves, buildings, ground surfaces, interfaces, other obstacles, and partial transmission through atmospheric structure), lack of wave coherence due to atmospheric turbulence, signal and measurement jitter in the UAV tones, statistical errors in front end time delay estimation and signal processing (e.g. the assumption of a stationary signal over the sampling period of a Fast Fourier Transform), wind noise and interference on ground microphones, UAV position and velocity errors, microphone location errors, variations in the sampling rate of the analog-to-digital converter (ADC) and uncertainty regarding moisture content in the atmosphere. We refer readers to (Spiesberger and Fristrup 1990, Ash and Moses 2005, Finn and Rogers 2015) for a more detailed understanding of the potential effects of these errors on the resulting tomographic inversions.

To generate the images below (Figure 3), errors were superimposed onto the 'true' value of time delay for each ray path, computed in accordance with (Finn and Rogers 2016) for the atmosphere in Figure 2. They were applied as a bias (representing errors due to refraction) and as separate additive Gaussian error functions (representing position errors for the UAV, position errors for the ground microphones, and timing errors due to front end signal processing, signal jitter, a lack of wave coherence, etc.). The components of error were: positional errors in the real time location of the UAV at each epoch (0.05m), positional errors in measuring the location of ground microphones (0.05m), errors due to signal processing, signal jitter, multi-path (0.1ms), and refraction errors (0.5% of true path length).

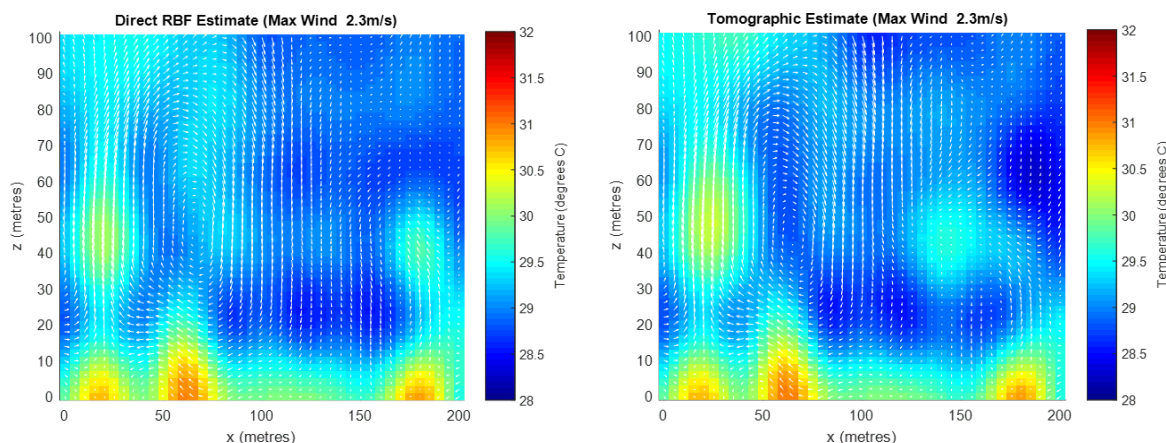


Figure 3: (left) a direct fit of RBF to the target LES data and (right) a tomographic reconstruction of the LES data based on simulated time delay observations with errors of 0.05m for UAV and microphone position, 0.1ms for signal processing uncertainty, and 0.1% path length for refraction. The RBF spacing is 20m x 20m. Microphone and ray path sampling regimes are as per Figure 2.

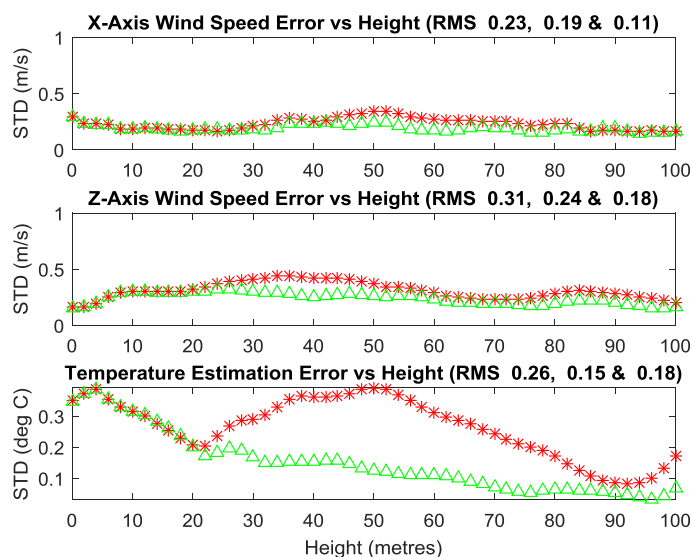


Figure 4: The direct (red stars) and indirect (green triangles) errors for Figure 3 and Figure 2

The mismatch between Figure 2 (left) and Figure 3 (right) represents what we refer to as the *direct* error, i.e. an indication of the degree to which the target (LES) data set can be accurately replicated using the inversion techniques. To a first order the direct error is driven by the density of the RBF lattice, which is driven by the stability of the inversion, i.e. singularities and noise in the residuals in the normal equations. Lower spatial resolution (fewer RBF) reduce the number of degrees of freedom (DOF) in the inversion process, which in turn tends to improve the ‘pose’ of the problem (a well-posed problem satisfies the following conditions: a solution exists, there is only a single solution, and this solution depends continuously upon the observations (Trampert 1999)).

Improving the pose of the problem means that errors in poorly estimated coefficients no longer propagate to others as the relationship is better constrained during the inversion process. We refer to the accuracy with which a tomographic inversion is able to faithfully represent RBF-spatially averaged LES data at the same density (resolution) of RBF as the *indirect* error. In other words, indirect error is the accuracy with which we can match Figure 3 (left)—a representation of the target data set using RBF at the density of the inversion RBF lattice—to Figure 2 (left), the actual target data set.

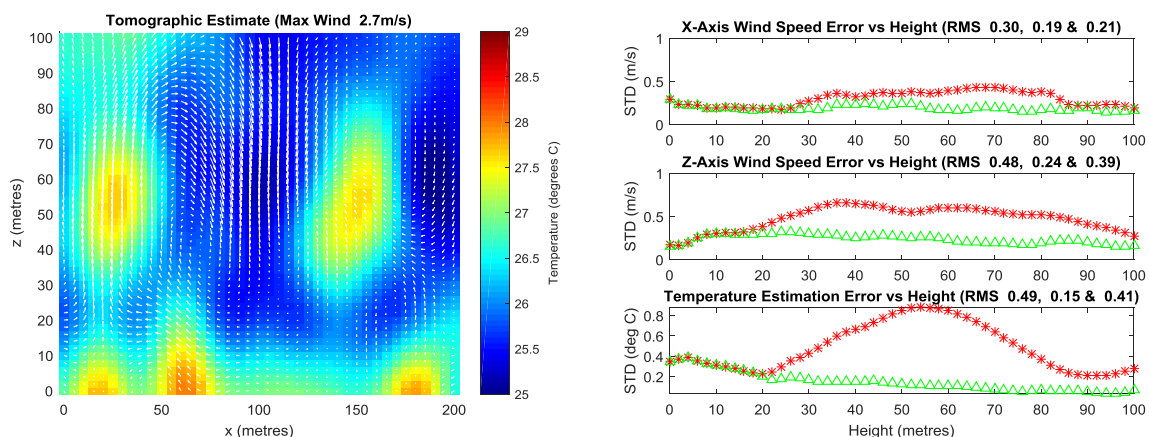


Figure 5: (left) a tomographic reconstruction of the LES data based on simulated time delay observations with errors of 0.05m for UAV and microphone position, 1ms for signal processing uncertainty, and 1% path length for refraction. The RBF spacing is 20m x 20m. Microphone and ray path sampling regimes are as per Figure 2. The right hand image shows the direct (red) and indirect (green) errors for Figure 3 (left) and Figure 2.

The direct errors in wind speed are 0.2-0.3m/s, whereas the indirect errors are 0.1-0.2m/s. The direct errors for temperature are approximately 0.3°, whereas the indirect errors are about 0.2°. When the input errors are increased to 1ms and 1% path length these direct and indirect errors increase to about 0.3-0.5m/s and 0.5°, indicating a likely upper practical limit to the accuracy requirements of the technique.

3. FIELD TRIALS

Field trials were conducted at an airfield at Saint Leonards, Victoria on the 10th and 11th of June, 2015. Both were overcast winter days with light or light-moderate winds. An Aerosonde MK 4.7 UAV was flown directly over a line of 28 microphones located adjacent to the main runway of the airfield. Each passage of the UAV was at constant height between 100m and 1,000m. The UAV travelled at approximately 28m/s and the array was set over a baseline of 575m. The duration of each overflight—the period when UAV was above the microphones—lasted about 20s (note: based on the detection and tracking ranges observed during the trials, UAV-based AAT appears to be effective over ranges/altitudes up about 1,700m).

The inter-sensor separation distances for microphones 1-9, 9-14, 14-15, and 15-29 were 25m, 5m, 50m (to span an intersecting runway), and 25m, respectively. All microphones were located approximately 1m above a flat grassy surface. The grass was about 3-4cm long and there was a change in elevation over the length of the array of about 3.7m. Each microphone was accurately located using Real Time Kinematic (RTK) Carrier Phase (CP) Differential Global Positioning System (DGPS).

The UAV is propelled by a twin cylinder 4-stroke engine with 2 exhaust mufflers: one for each cylinder. The exhausts are the major source of noise, although significant energy is also emitted by the engine, the rear mounted two-blade propeller, distributed aircraft vibration and aerodynamic noise. Each exhaust emits an exhaust pulse alternately for every second rotation of the engine. The mufflers are 106 mm apart. The UAV's acoustic emissions were sampled at 51.2kHz synchronously with the 1 pulse per second (PPS) reference of the GPS onboard the UAV.

The UAV was fitted with RTK CP DGPS, which enabled position recording with an accuracy better than 3cm at 20Hz. The GPS is located on the right wing, 850 mm from the aircraft centreline and is approximately 1m from the centre-point of noise emission. The GPS position recordings are corrected to reflect the location of the centreline of the UAV near the centre of gravity. The UAV recorded its own velocity over the ground at 20Hz, horizontal wind velocity and engine rotation rate at 1Hz and air temperature, mixing ratio, and specific and relative humidity at 0.2Hz.

The ground array comprised 28 ECM800 10mV/Pa condenser microphones sampled at 44.1kHz using four 8-channel 24 bit Data Acquisition (DAQ) recorders with 107dB spurious free dynamic range. The DAQ sampling frequencies drift with temperature and cannot be relied upon to provide accurate time-stamping. Hence, one of its channels recorded a GPS-derived 1 PPS signal to provide absolute timing reference, the remaining 7 channels recorded microphones. The accuracy of the combined signal time-stamping is thus approximately 22.5us.

A monostatic Fulcrum3D Sonic Detection and Ranging (SODAR), two Windmaster Ultrasonic 3D anemometers, four Hobo Pro v2 temperature and humidity sensors, and a Digitech Pro weather station were also deployed. All instruments were placed along the length of the microphone array, with the SODAR displaced perpendicularly from the array by about 35m. All were located using RTK CP DGPS. 3D wind velocity data was recorded at 10 Hz (Windmaster), temperature and humidity at 1Hz (Hobo Pro), and a broad range of standard meteorological parameters at 1/30Hz (Digitech Pro).

Acoustic pulses are transmitted by the SODAR, backscattered/reflected by temperature fluctuations in the refractive index of the atmosphere, and returned to the ground. As the reflected sound intensity depends strongly on the size of the fluctuations, scattering is restricted to patches of turbulence of scale size $\lambda/2$. The turbulent structures are assumed to move with the wind, so—as the Doppler shift effects the returned sound frequency—the radial components of wind velocity in the direction of the pulse may be measured. Vertical and horizontal components of wind speed can be computed for each height interval if beams are tilted off-vertical. To ensure there is adequate signal processing gain, a number of echoes are usually integrated over a period of minutes. This results in observations of wind velocity that are the vector sum of any time-stamped measurement.

The Fulcrum3D comprises 3 phased arrays, each with 37 piezoelectric transducers with 100% acoustic fill factor. The beams are physically set at 9° and 12.7° from vertical, with beam tilt independent of frequency (4,500Hz). 3D wind velocities are observed at 10m intervals between about 50m and 250m over an integration period of 10mins. The (1 σ) nominal uncertainty is 0.5m/s in each axis, but this figure is dependent upon the (integrated) signal returns and calculated for each data point.

The Hobo Pro v2 data were used as constraints in the inversion. The other instruments were used as independent (point) source of comparison for the reconstructions. The distribution of instruments along the sensor array is shown in Figure 6: white triangles show microphone positions, black triangles temperature and humidity sensors, black asterisks sonic anemometers, and the inverted “V” the location and nominal beam pattern of the SODAR.

The tomographic inversions were performed by modelling the temperature and wind fields as the sum of a uniform lattice of 7 horizontal by 5 vertical weighted Radial Basis Functions (RBFs), with the RBF centres located within the limits described by the flight path of the UAV and microphone array.

Figure 6 and Figure 7 show typical tomographic estimates derived from two UAV overflights, with the images in Figure 7 being observed about 110 seconds later than the ones in Figure 6. The UAV flew along the line of microphones (East-West and West-East) and at constant velocity and fixed altitude (425m and 475m) for Figure 6 and Figure 7, respectively. The left-hand images in both figures show wind velocities in the x-z plane plotted over a (vertical) temperature profile, colour-coded in accordance with the colour bar. The x-axis represents the baseline along the array of 28 microphones (with positive x oriented roughly due west and positive z oriented upwards). The right hand images of both figures show the x- and y-components of wind velocity in the x-z plane (superimposed onto the same x-z temperature profile), with positive y oriented roughly south, i.e. arrows pointing down indicate wind flowing out of the page (north). All images show wind vectors as scaled arrows, the maximum for which is 0.9 m/s for both left hand images—about a quarter of the way down Figure 6 and near the centre of Figure 7. The maximum wind speed (lower portion of right hand images) is about 1.8 m/s.

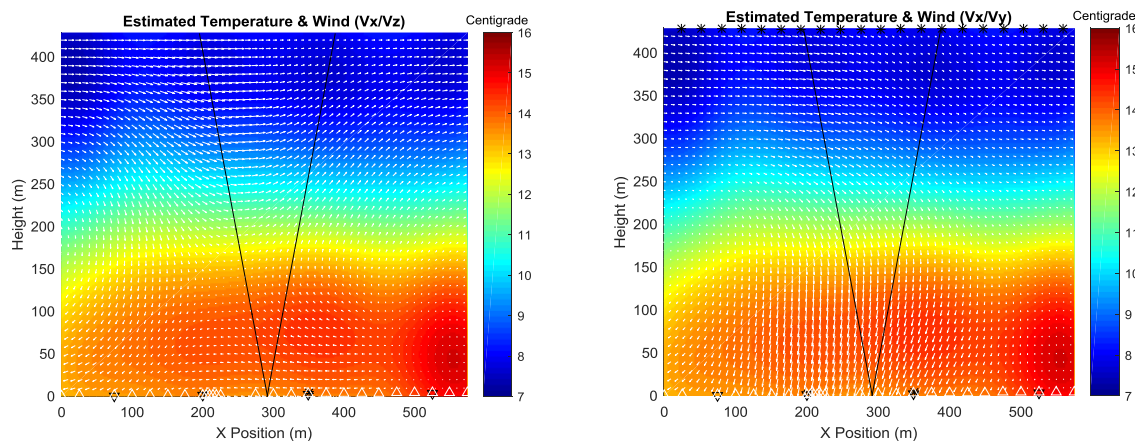


Figure 6: Tomographic estimates of scaled wind vectors and temperature in the (left) x-z and (right) x-y planes. White triangles show the microphone positions. Black triangles show the location of the Temperature and Humidity Sensors. Black asterisks show the locations of the sonic anemometers.

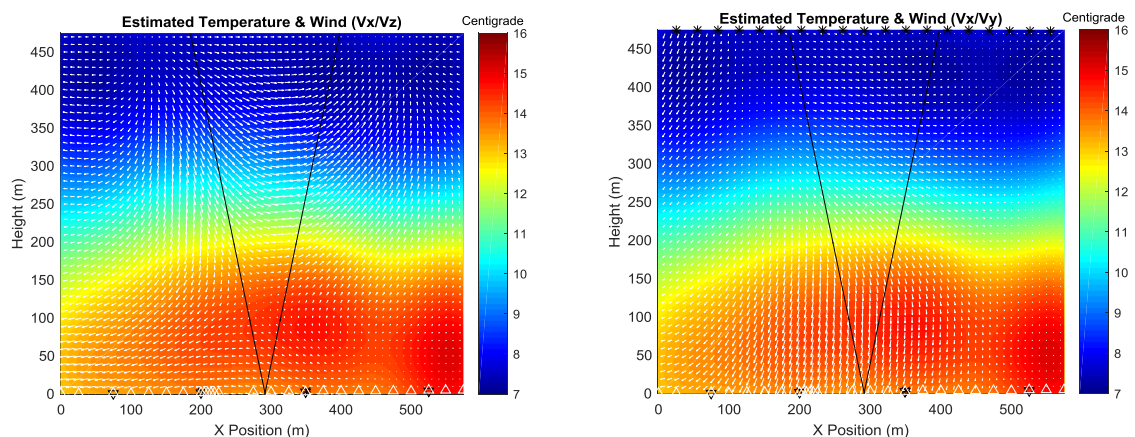


Figure 7: Tomographic estimates of scaled wind vectors and temperature in the (left) x-z and (right) x-y planes observed 110s after the images shown in Figure 6. The annotations are as per Figure 6.

Despite a 50 m increase in UAV altitude for the second overflight the temperature and wind profiles for both atmospheres are consistent. This provides considerable confidence in the computed inversions. The temperature drop is also consistent with typical adiabatic lapse rates.

Figure 8 (left) shows the wind speeds in each observed orthogonal component on the ground and at the UAV (which is only observed in the horizontal plane). The lower plots show the wind components observed by the anemometers, located at about 200m and 350m and shown as black asterisks in Figure 6 and Figure 7, whereas the upper image shows the wind speed components observed onboard the UAV. Figure 8 (right) shows the virtual temperature observed at the same locations, with the red lines in the lower plots representing a 5-point average of the raw data (blue lines). The observed data for the two flights, which last about 20 seconds each, correspond to the periods between about 15-35s and 125-145s.

Figure 9 shows a comparison between the tomographic estimates of Figure 6 and SODAR observations of wind velocity measured during the same period. The continuous lines represent estimates derived from the tomographic inversions, the circles represent observations from the SODAR. The upper images show wind speeds and the lower one wind direction in the horizontal plane (the vertical component of wind direction plane is not shown as the wind is so close to horizontal). In this instance, the SODAR only provided valid measurements between 70m and 210m, with standard deviations for each height shown as

error bars. For the sake of comparison, the tomographic estimates, which in Figure 6 and Figure 7 extend to 475m (but have been regularly observed up to heights/ranges in excess of 1.5km) were averaged at each height interval within the nominal beam width of the SODAR.

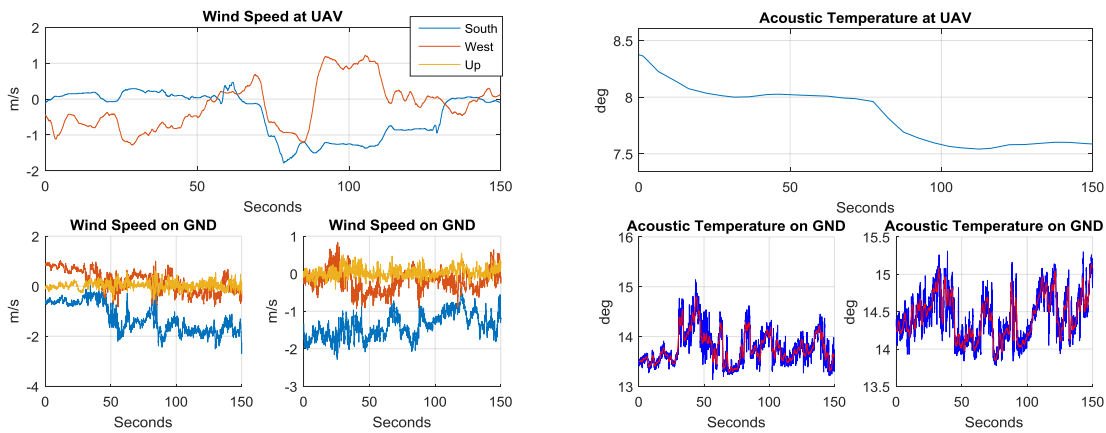


Figure 8: (left) wind speeds in each observed orthogonal component at the UAV (upper) and on the ground (lower) at both anemometer locations. Vertical wind speed is not measured/shown at the UAV; and (right) UAV and ground-based observations of acoustic/virtual temperature.

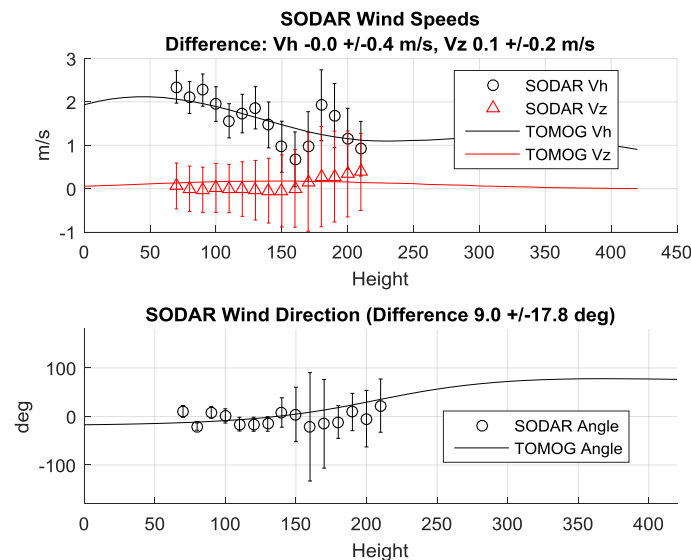


Figure 9: Comparison between SODAR measurements and tomographic estimates of wind velocity. The SODAR observations are ascribed to a vertical line roughly 35m from the plane described by the linear array of ground microphones and the UAV flight path.

Although the overall wind speed is very low, both data sets indicate that the magnitude of the horizontal wind speed falls from a maximum of around 2.2m/s at an altitude near 70m to just over 1.0m/s at 210m. The data sets also indicate a small (0.1m/s) vertical wind velocity above the SODAR. There is negligible mean difference between the two sets of data (< 0.1m/s) and rms difference of about 0.4m/s and 0.2 m/s in the horizontal and vertical planes. There is also close correspondence between the estimated directions of both data sets, with < 10° mean and 18° rms difference. These represent similar levels of relative accuracy to those observed between LIDAR, SODAR and traditional anemometry trials (Kelley, Jonkman et al. 2007).

4. CONCLUDING REMARKS

The LES-based simulations and preliminary results of the field trials analysis examined in this paper show that UAV-based tomographic methods show great potential for observing the temperature and wind velocity profiles of the atmospheric boundary layer. Detailed analysis of the correspondence between the different meteorological data sets is beyond the scope of this paper as experimental validation requires inter-comparison between the measurement sets to assess and calibrate the proposed technique relative to any variability and bias. It is anticipated that differences will be caused by three factors: spatial and temporal variability between observations, instrumentation differences (calibration, scattering and propagation mechanisms, instrumentation types, response times, etc.), and inaccuracies in any model-based interpolations. It is also possible that the SODAR may not have accurately observed the wind vectors due to their low velocity and vector summing during the integration.

Acoustic atmospheric tomography has practical application in a number of research fields, including boundary layer meteorology, land/sea surface-atmosphere interactions, theories of turbulence, and wave propagation through a turbulent atmosphere. For example—as the technique has advantages over more traditional point measurements that include its effect as a spatial filter for turbulence, the higher number of data per sensor, and minimal impact of the sensor devices on the observed atmosphere—it can be applied to the experimental validation of LES and microscale meteorological models of both convective boundary layer turbulence and the more stable nocturnal boundary layer.

5. REFERENCES

- Arnold, K., A. Ziemann and A. Raabe (1999). "Acoustic tomography inside the atmospheric boundary layer." *Phys. Chem. Earth, Part B: Hydrol., Oceans & Atmos.* **24**(1): 133-137.
- Ash, J. N. and R. L. Moses (2005). "Acoustic time delay estimation and sensor network self-localization: Experimental results." *J. Acoust. Soc. Am.* **118**(2): 841-850.
- Barth, M. and A. Raabe (2011). "Acoustic tomographic imaging of temperature and flow fields in air." *J. Meas. Sci. Technol.* **22**(3): 035102.
- Cornuelle, B. (1982). "Acoustic tomography." *Geoscience and Remote Sensing, IEEE Transactions on*(3): 326-332.
- Finn, A. and S. Franklin (2011). Acoustic sense & avoid for UAVs. *IEEE Proc. 7th Int. Conf. Intell. Sens., Sens Netw. Inf. Proc. (ISSNIP), 2011 IEEE*: 586-589.
- Finn, A. and S. Franklin (2011). UAV-based atmospheric tomography. *Proc. 2011 Australian Acoustical Society Conf.*
- Finn, A. and K. Rogers (2015). "The feasibility of unmanned aerial vehicle-based acoustic atmospheric tomography." *J Acoust Soc Am* **138**(2): 874-889.
- Finn, A. and K. Rogers (2016). "Acoustic Atmospheric Tomography Using Multiple Unmanned Aerial Vehicles (Accepted June 2016)." *IET Radar, Sonar & Navigation*.
- Finn, A. and K. Rogers (2016). "Improving Unmanned Aerial Vehicle-Based Acoustic Atmospheric Tomography by Varying the Engine Firing Sequence of the Aircraft." *Journal of Atmospheric and Oceanic Technology* **33**(4): 803-816.
- Finn, A., K. Rogers, J. Meade and S. Franklin (2014). Acoustic atmospheric tomography using multiple unmanned aerial vehicles. *Proc. SPIE Rem. Sens. Conf., International Society for Optics and Photonics*: 92420Q-92420Q-92428.
- Jovanovic, I., L. Sbaiz and M. Vetterli (2009). "Acoustic tomography for scalar and vector fields: theory and application to temperature and wind estimation." *J. Atmos. Oceanic Technol.* **26**(8): 1475-1492.
- Kak, C. and M. Slaney (2001). *Principles of computerized tomographic imaging*. Fred, Soc. Ind. Appl. Maths.
- Kelley, N. D., B. J. Jonkman, G. Scott and Y. L. Pichugina (2007). Comparing pulsed doppler LIDAR with SODAR and direct measurements for wind assessment, National Renewable Energy Laboratory.

- Kolouri, S. and M. R. Azimi-Sadjadi (2012). Acoustic tomography of the atmosphere using unscented Kalman filter. Proc. 20th Europ. Sig. Proc. Conf. (EUSIPCO), 2012 IEEE: 2531-2535.
- Munk, W. and C. Wunsch (1979). "Ocean acoustic tomography: A scheme for large scale monitoring." J. Deep Sea Res. - Part A. Ocean. Res. **26**(2): 123-161.
- Ostashev, V., A. Voronovich and D. K. Wilson (2000). Acoustic tomography of the atmosphere. IEEE Proc. Int. Geosci. Rem. Sens. Sym. (IGARSS 2000), IEEE. **3**: 1186-1188.
- R. Aster, B. B., C. Thurber (2013). Parameter Estimation and Inverse Problems. Maine, USA, Elsevier.
- Rogers, K. and A. Finn (2013). "3D UAV-based atmospheric tomography: Preliminary trials results." Proc. Aust. Acoust. Soc. Conference, Victor Harbour.
- Rogers, K. and A. Finn (2013). Frequency estimation for 3d atmospheric tomography using unmanned aerial vehicles. Proc. IEEE 8th Int. Conf. Intell. Sens., Sens. Netw. Inf. Proc., 2013 IEEE: 390-395.
- Rogers, K. and A. Finn (2013). "Three-Dimensional UAV-Based Atmospheric Tomography." J. Atmos. & Oceanic Techn. **30**(2): 336-344.
- Rogers, K. and A. Finn (2014). 3D acoustic atmospheric tomography. Proc. SPIE Conf. Rem. Sens., 2014, International Society for Optics and Photonics: 92420R-92420R-92429.
- Rogers, K. and A. Finn (2016). "Accurate sound speed estimation for unmanned aerial vehicle based acoustic atmospheric tomography (submitted 10 June 2016)." Journal of the Acoustical Society America TBA: 11.
- Spiesberger, J. L. and K. M. Fristrup (1990). "Passive localization of calling animals and sensing of their acoustic environment using acoustic tomography." Am. Naturalist: 107-153.
- Sullivan, P. P. and E. G. Patton (2011). "The effect of mesh resolution on convective boundary layer statistics and structures generated by large-eddy simulation." Journal of the Atmospheric Sciences **68**(10): 2395-2415.
- Trampert, R. S. a. J. (1999). Inverse Problems in Geophysics. New York, Springer Verlag.
- Vecherin, S. N., V. E. Ostashev, G. H. Goedecke, D. K. Wilson and A. G. Voronovich (2006). "Time-dependent stochastic inversion in acoustic travel-time tomography of the atmosphere." J. Acous. Soc. Am. **119**(5): 2579-2588.
- Vecherin, S. N., V. E. Ostashev and D. K. Wilson (2008). "Three-dimensional acoustic travel-time tomography of the atmosphere." Acustica **94**(3): 349-358.
- Vecherin, S. N., V. E. Ostashev, D. K. Wilson and A. Ziemann (2008). "Time-dependent stochastic inversion in acoustic tomography of the atmosphere with reciprocal sound transmission." J. Meas. Sci. Technol. **19**(12): 125501.
- Vecherin, S. N., V. E. Ostashev, A. Ziemann, D. K. Wilson, K. Arnold and M. Barth (2007). "Tomographic reconstruction of atmospheric turbulence with the use of time-dependent stochastic inversion." J. Acous Soc. Am **122**(3): 1416-1425.
- Wiens, T. and P. Behrens (2009). "Turbulent flow sensing using acoustic tomography." Proc. Inter-Noise 2009: Innov. Pract. Noise Control.
- Wilson, D., A. Ziemann, V. E. Ostashev and A. Voronovich (2001). "An overview of acoustic travel-time tomography in the atmosphere and its potential applications." Acustica **87**(6): 721-730.
- Wilson, K. D. and D. W. Thomson (1994). "Acoustic tomographic monitoring of the atmospheric surface layer." J. Atmos. Ocean. Technol. **11**(3): 751-769.
- Ziemann, A., K. Arnold and A. Raabe (1999). "Acoustic Travel Time Tomography—A Method for Remote Sensing of the Atmospheric Surface Layer." J. Meteorol. Atmos. Phys. **71**(1-2): 43-51.